1

Structural Studies in Perovskite Ferroelectric Crystals Based on Synchrotron Radiation Analysis Techniques

Jingzhong Xiao[1,2]
[1]*CEMDRX, Department of Physics, University of Coimbra, Coimbra,*
[2]*International Centre for Materials Physics, Chinese Academy of Sciences, Shenyang,*
[1]*Portugal*
[2]*China*

1. Introduction

Perovskite oxide materials, having the general formula ABO_3, form the backbone of the ferroelectrics industry. These materials have come into widespread use in applications that range in sophistication from medical ultrasound and underwater sonar systems, relatively mundane devices to novel applications in active and passive damping systems for sporting goods and automobiles [1-3]. Recent developments in regard to relaxor-based single crystal piezoelectrics, such as $Pb(Zn_{1/3}Nb_{2/3})O_3$–$PbTiO_3$ (PZNT), $Pb(Fe_{1/2}Nb_{/1/2})O_3$–$PbTiO_3$ (PFNT) and $Pb(Mg_{1/3}Nb_{2/3})O_3$–$PbTiO_3$ (PMNT) have shown superior performance compared to the conventional $Pb(Zr,Ti)O_3$ (PZT) ceramics[4, 5]. Particularly, their ultrahigh piezoelectric and electromechanical coupling factors in the <001> direction can reach to d_{33}>2000pC/N and k_{33}≈94%, which have attracted tremendous interests and still make these materials very hot.

However, the origin and structural nature of their ultrahigh performances remains one inquisitive but obscure subject of recent scientific interest.To better understand the structural nature of the outstanding properties, it is very important for investigating the ferroelectric domain structure in these materials. In ferroelectrics, according to the electrical and mechanical compatibility conditions, domain structures of 180^o and non-180^o will form with respect to crystal symmetry. There is a closely relationship between the domain structure and the crystal symmetry. Through the observation on ferroelectric domain configurations, the crystal structures can be confirmed. Ferroelectric domains are homogenous regions within ferroelectric materials in which polarizations lie along one direction, that influence the piezoelectric and ferroelectric properties of the materials for utilization in memory devices, micro-electromechanical systems, etc. Understanding the role of domain structure on properties relies on microscopy methods that can inspect the domain configuration and reveal the evolution or the dynamic behaviour of domain structure.

It is also well known that the key to solve this issue of exploring the origin of the excellent properties is to reveal the peculiar complex perovskite crystal structures in these materials. Through study in structure behavior under high-pressure and local structure at atomic level will be helpful for better understanding this problem.

2. Synchrotron radiation X-ray structure investigation on ferroelectric crystals

$Pb(Zn_{1/3}Nb_{2/3})O_3$-$PbTiO_3$ (PZNT) and $Pb(Fe_{1/2}Nb_{/1/2})O_3$–$PbTiO_3$ (PFNT) crystal are model ABO_3-type relaxor ferroelectric materials (or ferroelectrics), which demonstrates excellent performance in the filed of dielectrics, piezoelectrics, and electrostriction, etc. To explore the common issues of structural nature and the relationship between structure and performance of ultrahigh-performance in these materials, in this chapter, the novel X-ray analysis techniques based on synchrotron radiation light, such as synchrotron radiation X-Ray topography, high-pressurein situ synchrotron radiation energy dispersive diffraction, and XAFS method, are utilized to investigate the domain configuration, structure and their evolution behavior induced by temperature changes and external field.

2.1 Application of white beam synchrotron radiation X-ray topography for in-situ study of ferroelectric domain structures

Ferroelectric domains can be observed by various imaging techniques such as optical microscopy, scanning electron microscopy (SEM), transmission electron microscopy (TEM), X-ray imaging, and etc. Imaging is normally associated with lenses. Unlike visible light or electrons, however, efficient lenses are not available for hard X-rays, essentially because they interact weakly with matter. Comparatively as an X-ray imaging method, X-ray topography plays a vital role in providing a better understanding of ferroelectric domain structure.[6] X-rays are more penetrating than photons and electrons, and the advent of synchrotron radiation with good collimation, a continuous spectrum (white beam) and high intensity has given X-ray topography additional powers. The diffraction image contrast in X-ray topographs can be accessed from variations in atomic interplanar spacings or interference effects between X-ray and domain boundaries so that domain structure can be directly observed (with a micrometer resolution). Especially, via a white beam synchrotron radiation X-ray diffraction topography technique (WBSRT), one can study the dynamic behaviour of domain structure and phase evolution in ferroelectric crystals respectively induced by the changes of sample temperature, applied electric field, and other parameter changes.
In this chapter, a brief introduction to principles for studying ferroelectric domain structure by X-ray diffraction imaging techniques is provided. The methods and devices for in-situ studying domain evolution by WBSR are delineated. Several experimental results on dynamic behavior of domain structure and induced phase transition in ferroelectric crystals accessed at beam line 4W1A of the Beijing Synchrotron Radiation Laboratory (BSRL) are introduced.

2.1.1 Principle of synchrotron radiation X-ray topography

a. X-ray topography approach

X-ray diffraction topography is an imaging technique based on Bragg diffraction. In the last decades, X-ray diffraction topography to characterize crystals for the microelectronics industry were developed and completely renewed by the modern synchrotron radiation sources. [6]
Its images (topographs) record the intensity profile of a beam of X-rays diffracted by a crystal. A topograph thus represents a two-dimensional spatial intensity mapping of reflected X-rays, i.e. the spatial fine structure of a Bragg spot. This intensity mapping reflects the distribution of scattering power inside the crystal; topographs therefore reveal the

irregularities in a non-ideal crystal lattice. The basic working principle of diffraction topography is as follows: An incident, spatially extended X-ray beam impinges on a sample, as shown in Fig.1. The beam may be either monochromatic, or polychromatic (i.e. be composed of a mixture of wavelengths (white beam topography)). Furthermore, the incident beam may be either parallel, consisting only of rays propagating all along nearly the same direction, or divergent/convergent, containing several more strongly different directions of propagation.

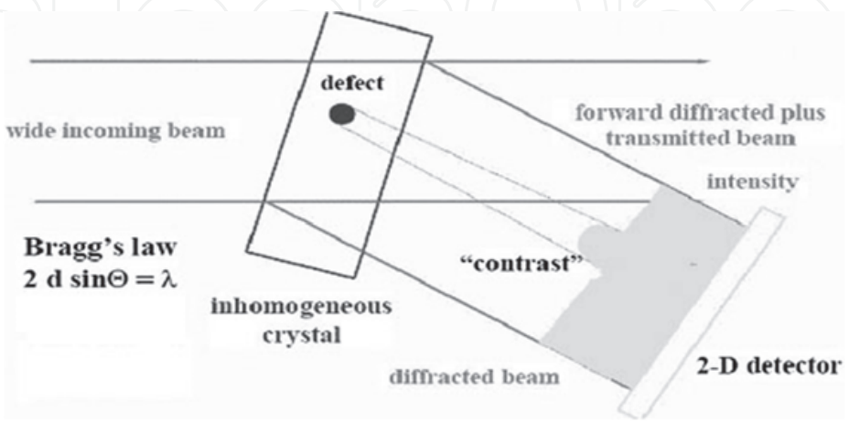

Fig. 1. The scheme of basic principle of diffraction topography.

A homogeneous sample (with a regular crystal lattice) would yield a homogeneous intensity distribution in the topograph (a "flat" image). Intensity modulations (topographic contrast) arise from irregularities in the crystal lattice, originating from various kinds of defects such as cracks, surface scratches, dislocations, grain boundaries, domain walls, etc. Theoretical descriptions of contrast formation in X-ray topography are largely based on the dynamical theory of diffraction. This framework is helpful in the description of many aspects of topographic image formation: entrance of an X-ray wave-field into a crystal, propagation of the wave-field inside the crystal, interaction of wave-field with crystal defects, altering of wave-field propagation by local lattice strains, diffraction, multiple scattering, absorption. Theoretical calculations, and in particular numerical simulations by computer based on this theory, are thus a valuable tool for the interpretation of topographic images. Contrast formation in white beam topography is based on the differences in the X-ray beam intensity diffracted from a distorted region around the defect compared with the intensity diffracted from the perfect crystal region. The image of this distorted region corresponds to an increased intensity (direct image) in the low absorption case.
To conduct a topographic experiment, three groups of instruments are required: an x-ray source, potentially including appropriate x-ray optics; a sample stage with sample manipulator (diffractometer); and a two-dimensionally resolving detector (most often X-ray film or camera). The x-ray beam used for topography is generated by an x-ray source, typically either a laboratory x-ray tube (fixed or rotating) or a synchrotron source. The latter offers advantages due to its higher beam intensity, lower divergence, and its continuous wavelength spectrum. The topography technique combinning with a synchrotron source, is well adapted to in-situ experiments, where the material, in an adequate sample environment device, is imaged while an external parameter (temperature, electrical field, and etc) is changed.

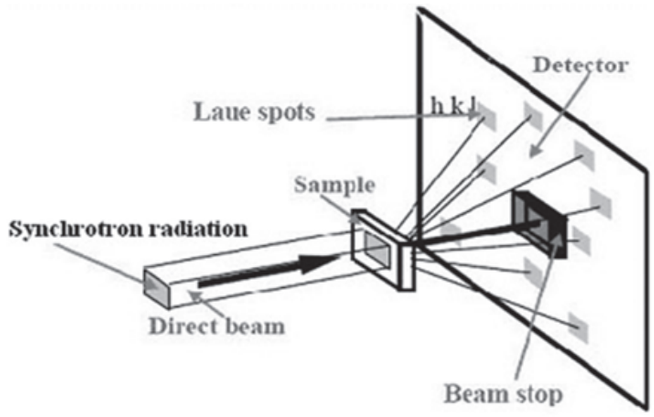

Fig. 2. Experimental arrangement for synchrotron radiation white beam Laue topography.

b. White beam X-ray topography

A simple way to understand the creation of X-ray topographic images is to consider a Laue photograph (Fig. 2). A polychromatic (white) X-ray beam, containing X-ray energies from about 6 keV to 50 keV (X-ray wavelengths from approximately 2 Å to 0.25 Å), impinges on a crystal. [6] The beam is diffracted in many directions, creating Laue spots. The positions of the diffraction spots appear according to the Bragg equation:

$$E = \frac{hc}{2d\sin\theta_B}, \text{ or } \lambda = 2d\sin\theta_B \tag{1}$$

where E is the incident X-ray energy (and λ is the incident wavelength) selected by crystal planes with spacing d, h is Planck's constant, c is the speed of light, and θ_B is the Bragg angle. Each spot contains uniform intensity if the crystal is perfect.

If, however, the crystal is strained, streaks appear instead of spots due to variations in lattice spacing. In fact, each Laue spot contains a spatial distribution of diffracted intensity attributable to the presence of defects in the crystal. This distributed intensity is difficult to see because Laue spots are typically the same size as the X-ray beam pinhole, and the incident X-ray beam is divergent, but each tiny Laue spot is actually an X-ray topograph. At synchrotron radiation facilities, a collimated white X-ray beam can be used to illuminate a sample crystal, and spots with the much larger cross section of the synchrotron X-ray beam are recorded. The resulting data are an array of Laue spots, as shown in Fig. 2, each of which is an X-ray topograph arising from a different set of atomic planes.

c. Ferroelectric domain characterizations

The existence of antiparallel 180° domains is one of the fundamental properties of ferroelectrics and direct observation of these domains is invaluable to the understanding of the polarization reversal mechanism of ferroelectric structures. Among the techniques of visualizing antiparallel domains, conventional x-ray topography is an important and efficient method although its application is limited by the only available characteristic radiations. However, this limitation is easily overcome by the white-beam synchrotron radiation topography (WBSRT). A unique aspect of WBSRT is the opportunity it affords to select out of the continuous spectrum any intended wavelengths to activate strong anomalous scattering. And, with the WBSRT, it is possible for several diffraction images

with anomalous dispersion effect to be activated simultaneously so that the contrast reversal of 180° domains can be directly observed.[7-9] The natural collimation and high intensity of the radiation also make the real-time observation of domain dynamics feasible. As shown in Fig.3, when working with a coherent x-ray beam, and if the phases of the structure factors are different, the 180° ferroelectric domains can be revealed.

Considering the mechanical and electrical compatibility conditions, allowed domains in ferroelectrics are the 180o or non-180o ones with the different planes as the domain walls.[8, 9] The extinction condition for a domain wall is:

$$\Delta P \bullet g = 0 \tag{2}$$

where g is the reciprocal vector of the diffracting plane, $\Delta P = P_1 - P_2$ is the difference of the polarization vectors across the domain wall. Non-180° domain structure is illustrated in Fig.4.

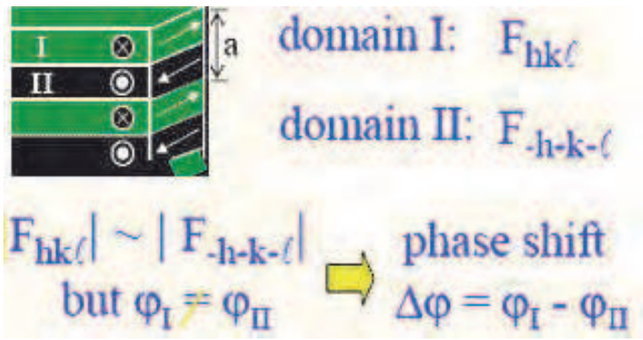

Fig. 3. (Colour on the web only) Scheme of 180° domain.

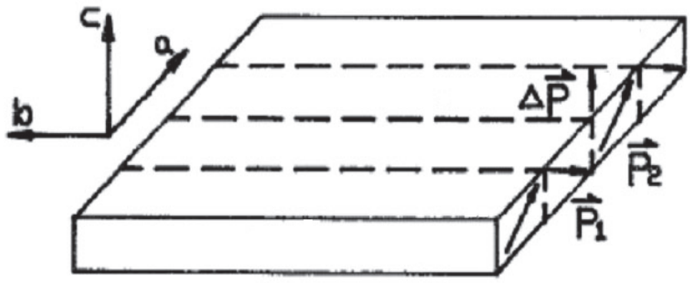

Fig. 4. Scheme of non-180° domain.

2.1.2 In-situ topography measurements

White beam synchrotron radiation topography not only overcomes the drawback of long exposure time for the conventional x-ray topography, but also extends the scope of topography study. The excellent collimation and high intensity of the synchrotron radiation makes the possibility of enlarging the distance between the light source and sample, to improve the image resolution and enlarge the distance between the sample and the detector. These allow ones able to install the samples inside large environmental chambers with changes of temperature, electric field, or other parameters, to carry out the in-situ topography studies. [10]

a. High temperature condition

A high-temperature chamber was used for in situ topography study. The cylindrical furnace in use was made of pure graphite. Two beryllium windows were used for incident and outgoing x-rays. Two thermocouples attached close to the specimen were used to monitor and control the temperature. A digital control power supply can ramp the electric current smoothly when starting to heat. The temperature control system is based on the Eurotherm controller (model 818) and solid state relay (SSR). By using PID control and time proportion method, the temperature stability is about 0.05°C when holding and 0.1°C when ramping. The on-line PC can set and monitor the temperature via RS-232 interface. A sketch of this chamber is shown in Fig. 5.

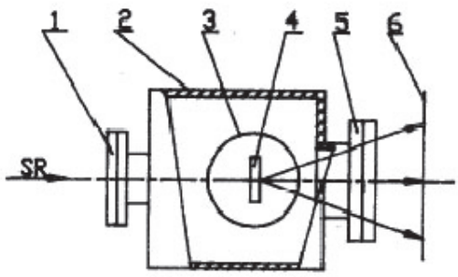

Fig. 5. Sketch of the high temperature sample chamber: 1-entrance Be window; 2-water cooling environment chamber; 3-furnace; 4-specimen; 5-exit Be window; 6-film.

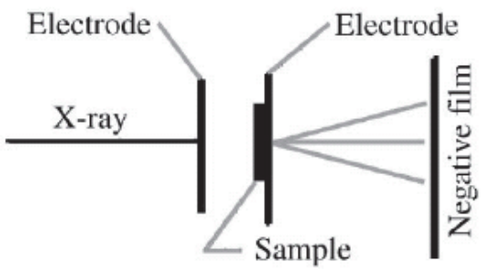

Fig. 6. The experimental arrangement for applying electric field.

b. DC electric field

The change of the ferroelectric domain structure due to the applied DC field can also be observed by white beam synchrotron radiation topography. Fig. 6 is the experimental arrangement of applying the DC field. The distance between the two electrodes was 4 mm and the applied DC voltage ranged from 0 to 4400 V. The samples can be installed on the surface of plastic plates. The DC electrical field can be applied on two Al electrodes covering on the surface of two X-ray transparent organic materials.

2.1.3 In-situ topography study in ferroelectric crystals

The in-situ experiments are performed at Beijing Synchrotron Radiation Facility (BSRF). The x-ray topography station and attached 4W1A beamline are part of the BSRF. The 4W1A is a 45m long white/monochromatic wiggler beamline. When the BEPC is operated at the

energy of 2.2 GeV and the magnetic field of the wiggler at 1.8T. The topography station situated at the end of the beamline 4W1A is mainly used for the study of the perfection of single crystals, high resolution multi-crystal diffraction and x-ray standing wave research. The main equipment of the station consists of a white radiation topography camera, three environmental sample chambers, an x-ray video imaging system and a four crystal monochromatic camera.

The white radiation topography camera and three environmental sample chambers are used for the dynamic topographic experiments with change of temperature, stress, electric field or other parameters. The white radiation camera has five axes to rotate the specimen to any orientation with the incident beam and to rotate the detector to collect the any diffracted beam.

a. Domain and temperature-induced phase transformation in 0.92Pb ($Zn_{1/3}Nb_{2/3}$)O_3–0.08$PbTiO_3$ crystals

The aim of this present work is to investigate temperature-dependence phase evolution in 0.92Pb ($Zn_{1/3}Nb_{2/3}$)O_3–0.08$PbTiO_3$ (PZN–8% PT) crystals, by employing a real time white-beam synchrotron X-ray radiation topography method (WBSRT). By combining this technique with other complementary structural experiments, a novel picture of low symmetry phase transformation and phase coexistence is suggested.

PZN–8% PT single crystals used in this experiment were grown by the PbO flux method. A plate perpendicular to [001] axis is cut and well polished to approximately 200 μm in thickness. Real time observation is performed at the topography station at the 4W1A beam line of Beijing Synchrotron Radiation Laboratory (BSRL). The storage ring is 2.2 GeV with beam current varied from 50 mA to 90 mA. A cylindrical furnace with coiled heating elements arranged axially around the sample space is used for in situ topography investigation. After carefully mounted the samples on the hot-stage, we heat them at a slow rate of 0.5 ^oC/min, observe and record the dynamic topography images by photo films. Through the topography images obtained by this method, we can clearly observe the ferroelectric domain configurations and their evolution as a function of temperature in PZN–8% PT crystals.[11]

Fig. 7 shows a series of synchrotron radiation topography images with (112) reflection of the (001) crystal plate taken at different temperatures. From Fig. 7 (a) to (i), we find that the domain structures are very complex. They can be categorized into three kinds of domains and addressed as A, B, and C, as shown in Fig. 7 (j).

The A domain walls, which are at approximately 45^o to the [100] axis, can be obviously observed at room temperature. These domain walls are considered to be the 71^o (or 109^o) ones in rhombohedral PZN–PT crystals, and can be clearly observed before heating the sample to 132 ^{o}C. With increasing temperature from 75 ^{o}C to 131 ^{o}C, as shown in Fig. 7 (b)–(c), the B domain laminates become progressively obvious and coexist with the A domains. On the other hand, these domain laminates are along the [010] axis, which can be classified into 90 ^{o} tetragonal domain walls. At the point of 131 ^{o}C, the tetragonal domains become most clear. With heating the sample to above 132 ^{o}C, as shown in Fig. 7 (d), we find that the rhombohedral 71 ^{o} (or 109 ^{o}) domain walls (A laminates) become vague, and the image background becomes brighter than before. However, the tetragonal domain walls are still clear. This phenomenon shows that the phase transition from rhombohedral to tetragonal phase (R–T transition) starts at 75 ^{o}C, and the tetragonal domains grow gradually.

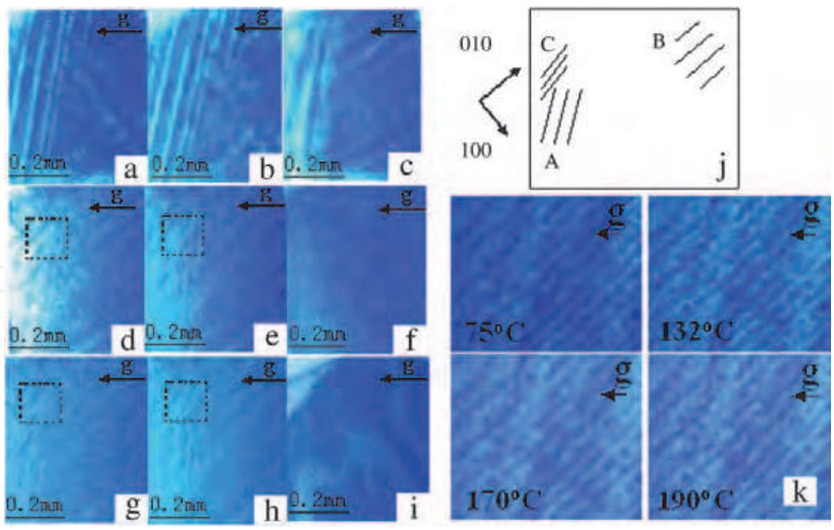

Fig. 7. (Colour on the web only) Images of the in situ synchrotron radiation topography in PZN–8% PT crystals, the x-rays incident direction to the crystal is [001], the diffraction vector is g = (112): (a) room temperature (20 °C); (b) heating to 75 °C; (c) heating to 131 °C; (d) heating to 132 °C; (e) heating to 190 °C; (f) heating to 262 °C; (g) cooling to 190 °C; (h) cooling to 75 °C; (i) cooling to room temperature; (j) Schematic picture for presenting the ferroelectric domain configurations in the topography images of PZN–8% PT crystals; (k) enlarged images of C domain walls from 75 °C to 190 °C.

Most particularly, a set of unique domain walls (C domain walls) appear at this temperature, which is quite different from the A and B domains. This kind of domain walls is shown in Fig.7 (k), through the enlarged images taken from 75 °C to 190 °C. As the figures show, the C domain laminates deviate from the (010) direction at 15 °–20 °. According to the knowledge of domains orientation in crystals with different symmetry and X-ray diffraction extinction relations, as formula (2) shows, these laminates can be considered to be neither rhombohedral nor tetragonal domain structures, but a new monoclinic phase domain structure.

With further heating of the system to about 132 °C, we find this domain structure is very stable and coexists with B tetragonal domains. Upon further heating to above Tc (170 °C), the monoclinic C domain structure also remains. This case shows that a monoclinic phase not only appears in the process of ferroelectric–ferroelectric phase transformation, but also coexists with the cubic phase well above TC . With the temperature elevating to about 262 °C, we find nearly all the ferroelectric domains disappear, as shown in Fig. 7 (f).

Whilst cooling the sample from 262 °C to 75 °C, the monoclinic domains (C laminates), as well as the tetragonal domains (B laminates), are found to reappear, whereas the rhombohedral domains (A laminates) cannot be recovered by cooling to room temperature. During the crystal growth, a rapid cooling process was employed for quick crystallization and to avoid the generation of a pyrochlore phase, which results in a strain field in the crystal. The rhombohedral A domains are expected to be induced by this kind of strain field and preserved at room temperature. Thus A domains do not reappear after the crystals are re-cooled from 260 °C to room temperature with a slow cooling rate, since this cooling process possibly releases the crystal strain field. However, the monoclinic phase was not generated by the strain field induced during the crystal growth, since the particular C domains as well as B domains can be recovered at 75 °C by slow cooling.

Generally, with the sample temperature reaches to the Curie temperature, there occurs a ferroelectric-paraelectric phase transition in conventional ferroelectrics, which results in the disappearance of the domain structure. However in relaxor ferroelectrics, as shown in Fig. 8 the domain structure can be observed clearly on (111) face of PZN-8%PT crystal when the sample temperature is much higher than the Curie temperature. This phenomenon can be induced by the micro-polarization-region in relaxor crystals.
Through in situ synchrotron radiation topography under various temperatures, the complex configuration and dynamic evolution of ferroelectric domains in ferroelectric crystals are obtained. It is expected that the present results will encourage more research interest in exploring the origin of the ultra-high piezoelectric and electrostriction properties in ferroelectrics and other advanced materials.

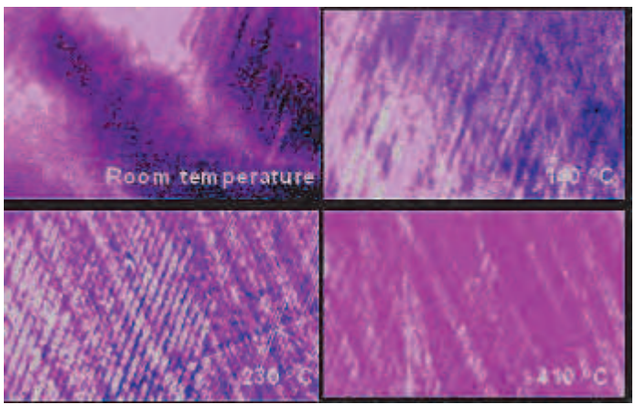

Fig. 8. (Colour on the web only) The temperature induced evolution of the domain structure on (111) face of PZN-8%PT crystal, observed by in situ synchrotron radiation topography.

b. Electrical field induced domain structure

The $Gd_2(MoO_4)_3$ (GMO) crystals were grown by the induction-heated CZ technique. The (0 0 1) crystal pieces of 10 – 15mm diameter were cut and polished into 2.0 or 0.5mm in thickness. The transparent pieces were using to study the DC electric field induced domain structure by transmission X-ray topography at beam line 4W1A of the Beijing Synchrotron Radiation Laboratory (BSRL) The change of the domain structure due to the applied DC field was also observed. Fig. 6 is the experimental arrangement of applying the DC field. The distance between the two electrodes was 4mm and the applied DC field ranged from 0 to 4400 V.

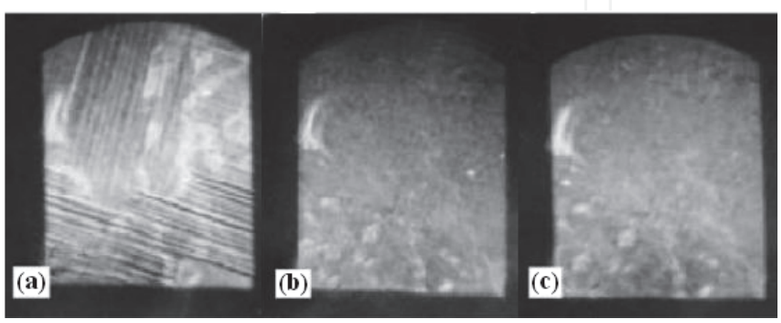

Fig. 9. The domain structure of GMO varies with the applied DC field.

Fig. 9 is a set of series topographs when an applied DC field was added on the GMO crystal piece. Fig. 9 (a) and (b) are the results obtained when the applied voltage was 600 and 700 V, respectively, and the domain structure did disappear. Fig. 9 (c) was the result when the voltage was lowered to zero. From these photographs, we concluded that the multidomain could be transformed to single domain by applying a DC field and that the single domain could be kept even if the applied DC field was taken away. This experimental result shows us that it is possible to make a periodically poled GMO crystal, despite the presence of ferroelectric and ferroelastic domains in the unpoled GMO crystal. From these results, we concluded that the ferroelectric and ferroelastic multidomains could be transformed to a single domain by the applied DC field, and the single domain could be kept even if the applied DC field was taken away.[12]

2.2 High-pressure structural behavior in PZN-PT relaxor ferroelectrics

The ideal structure of ABO_3-type perovskite can be described as a network of corner-linked octahedra, as shown in Fig.10. With *B* cations at the centre of the octahedra and *A* cations in the space (coordination 12) between the AO_{12} and BO_6 polyhedra. As its *B* cation comprised by Zn^{2+}, Nb^{5+}, and Ti^{4+} ions, as well as the *A* cation comprised by Pb^{2+} ion, PZNT deviates from the ideal perovskite by cation displacements or a rotation (or tilting) of BO_6 octahedra. The possible ''off-centering'' of the *B* cations makes the crystal structure more complex than that of the ideal ABO_3-type perovskites and reasonably influence the properties. Previously, approaches towards the understanding of the relaxor ferroelectrics were focused on the structural evolution induced by the changes of chemical composition, electrical field or temperature environment.[13-14] Virtually, these above variables induce phase transitions by mainly playing a role of causing displacement of the cation and anion and rotation of BO_6 octahedra in perovskite.

Nevertheless, directly compressing the materials can also induce similar results that will provide a new ken and approach to investigate the complex structure in the ferroelectrics and other functional materials. It is pointed out that the effect of pressure is a ''cleaner'' variable, since it acts only on interatomic interactions.[15] Compared to other parameters, as an extreme variable, high-pressure is of the unique importance in elucidating ferroelectrics, for the unique structural change is susceptible to pressure. Studying the structural changes and compressive behaviors under high-pressure condition is able to facilitate the understanding for structural nature of the high-performances in relaxor ferroelectrics or other novel functional materials under normal state. Thus, recently, the high-pressure structural investigations in relaxor ferroelectrics had become very popular.[16,17] For instance, Kreisel, et al performed a high-pressure investigation by Ramman spectroscopy of $Pb(Mg_{1/3}Nb_{2/3})O_3$ (PMN), and had obtained the unusual pressure-dependent Ramman relaxor-specific spectra and phase change. By combining the external parameter high pressure with x-ray diffuse scattering method, a pressure-induced suppression of the diffuse scattering in PMN was indicated. Their observed pressure-induced suppression of diffusesed scattering above 5GPa is also a general feature in relaxors at high pressure.[18] In this present work, we performed a high-pressure synchrotron radiation energy-dispersive x-ray diffraction (EDXD) investigation on 0.92PZN-0.08PT ferroelectrics, to study the compressive behavior of the materials under high-pressure condition.

Fig. 10. Illustration of ideal ABO_3-type perovskite structure, which can be described as a network of corner-linked octahedral.

2.2.1 High-pressure synchrotron radiation energy-dispersive x-ray diffraction (EDXD)

The high-pressure X-ray diffraction patterns employed an energy-dispersive method and were recorded on the wiggler beam line (4W2) of the Beijing Synchrotron Radiation Laboratory (BSRL).[19] A WA66B-type diamond anvil cell (DAC) was driven by an accurately adjustable gear-worm-level system. The 0.92PZN-0.08PT powders and pressure calibrating materials (Platinum powder) were loaded into the sample chamber of a T301 stainless steel gasket. A mixture of methanol/ ethanol 4:1 was used as the pressure medium. Pressure was determined from (111), and (220) peaks of Pt along with its respective equation of state. The *d*-values of the specimens can be obtained according to the energy dispersion equation:

$$E \cdot d = \frac{0.619927}{\sin\theta}(keV \cdot nm) \tag{3}$$

The polychromatic X-ray beam was collimated to a 40×30 μm sized spot with the storage ring operating at 2.2 G eV. The diffracted beam was collected between 5 and 35 k eV and the diffraction 2θ angle between the direct beam and the detector was set at about 15.9552 °. The experiment setup is shown in Fig. 11. The pressure-induced crystallographic behavior was studied up to 40.73GPa at room temperature in 22 steps during the pressure-increasing process, and the evolution of high-pressure EDXD patterns is obtained.

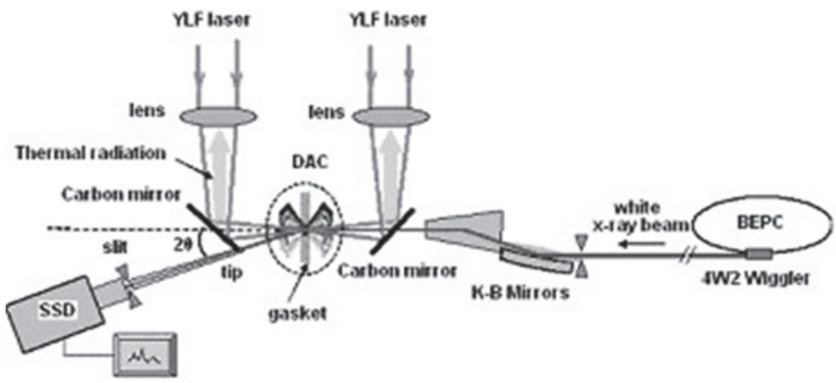

Fig. 11. The setup of high-pressure X-ray energy-dispersive diffraction experiment.

2.2.2 High-pressure compressive behavior in PZNT-PT crystals

Fig.12 shows the selected EDXD patterns of 0.92PZN-0.08PT sample under different pressures, from which the peaks of (110), (111), (200), (210), and (211) indexed in terms of rhombohedral structure can be observed. The strong peaks of (111) and (200) of Pt, whose photonic energy is 19.72keV and 22.77keV respectively, will also be clearly observed. Apart from these diffraction lines, several fluorescence peaks of Pb and Nb are emerged in the low-energy side of the curve.

With increasing pressures from the ambient pressure (0 GPa), the (110) and (200) peak become broader, the intensity of (210) and (211) peaks start to decrease from 5.17GPa. On further increasing pressure, the intensity of (210) and (211) peaks become weaker from 21.34GPa, and the (210) peak vanishes at the pressure of 28.38 G Pa. at about 40.73GPa, these two peaks seem to be vanished. The abrupt changes of the EDXD patterns indicates that the phase transitions can possibly be induced by applying pressures, and the estimated transition pressure point is at about 5.17GPa and 28.38GPa, respectively.

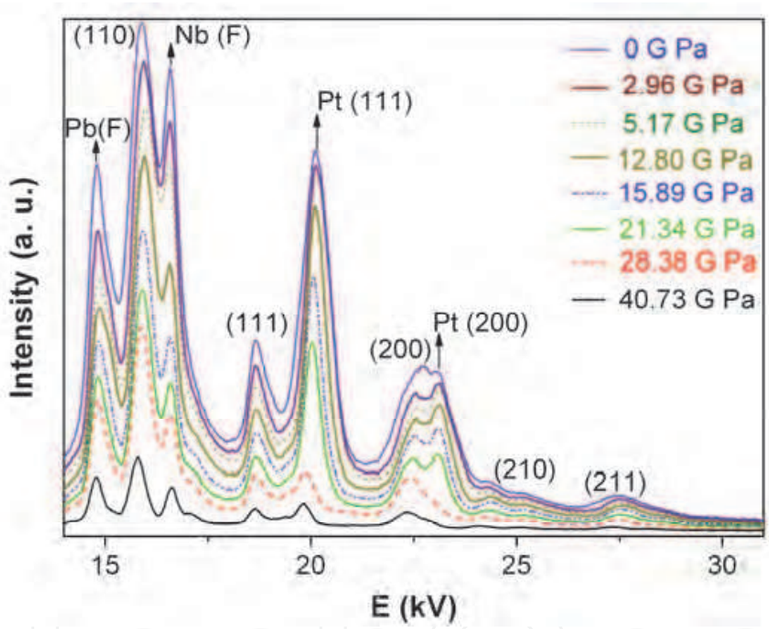

Fig. 12. (Colour on the web only)The EDXD curves of PZNT sample under different pressures, the maximum pressure applied here is 40.73 G Pa. Pb (F) and Nb (F) indicate the fluorescence peaks of Pb and Nb emerged in the low-energy side.

In order to better understand the pressure-induced phase transition and compressive behavior of 0.92PZN-0.08PT, we calculated the structure parameters such as interplanar spacing value (d-value) evolving under various pressures according to experiment results and equation (1), as shown in Fig.13. It is noticed that, as a function of pressure, the d-value decreasing issues of different peaks of (110), (200), and (211) are greatly different, reveals that the compressibility of structural parameters is anisotropic. To investigate the compression behavior of the sample in different pressures, we divided the $d_{(110)}$ vs. pressure curve into several zones. It shows the decreasing rate of $d_{(110)}$ spacing in different pressure zones is different, i.e., the decreasing rate of the zones of *A*, *C*, *E*, and *G* are not identical, which should demonstrate that the change of compressibility is also nonlinear.

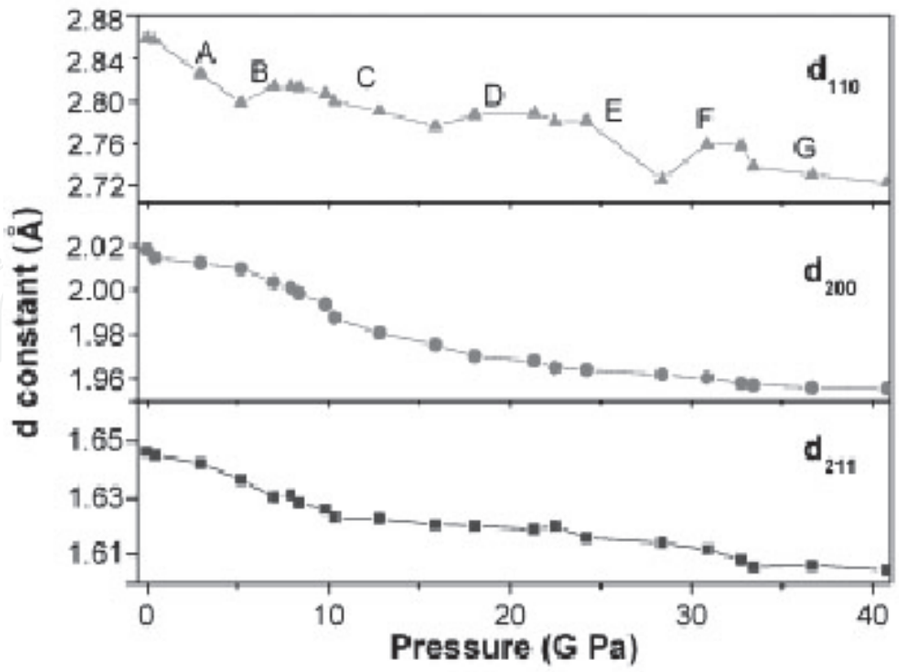

Fig. 13. The curves of d-spacing parameters of different diffraction peaks under various pressures. Top part: $d_{(110)}$ vs. pressure; Middle part: $d_{(200)}$ vs. pressure; and Bottom part: $d_{(211)}$ vs. pressure.

The abrupt changes appeared in *B*, *D*, and *F* zones of the curve, which are corresponding to the three pressure ranges of about 5.17-7.5GPa, 15.2GPa-21.4GPa, and 30.3-34.5GPa, respectively, showing several kinky ranges.[20] We name this phenomenon as "multi-kinky" pressure behavior. This behavior is considered not to be induced by the measurement errors according to the error analysis. Generally, the energy resolution of the detector in EDXD experiment is a key parameter to determine diffraction peak position. In the present experiment, Si (Li) detector is adopted and its energy resolution is estimated to be about 170 e V, from which the measuring error of diffraction peak position may be calculated to be less than 3 eV, corresponding to a relative measuring error of structural parameter of $(\Delta d/d) \approx 10^{-4}$. But for instance, in Fig.13a, the calculated $(\Delta d/d)$ of the (110) face in kinky ranges is estimated to be at the order of 10^{-2}. Therefore, the abnormal change of *d*-spacing under high-pressure should be intimately related to the structural characteristics of ABO_3 compounds. Particularly, in *B* and *D* zones, the $d_{(110)}$ value firstly increases and then decreases with the applied pressures, which seems to show a abnormal compressive behavior. While in *F* zone, the $d_{(110)}$ value decreases with the increased pressure. This behavior can be ascribed to the abruptly changed strain induced by structural transformation from phase *E* to the phase *G*. The *B*, *D*, and *F* zones can also be considered as the areas for phase-coexistence, or transformation regions.[21] The d-spacing vs. pressure curves of (200) and (211) peaks also exhibit multi-kinky changes and nonlinear compressive behavior. Therefore, it is estimated that this multi-kinky behavior is indicative of pressure-induced multi-phase transition and phase coexistence occurs in 0.92PZN-0.08PT crystals. The accurate pressure-induced lattice changes extracted from the high-pressure EDXD experiments will be published elsewhere.

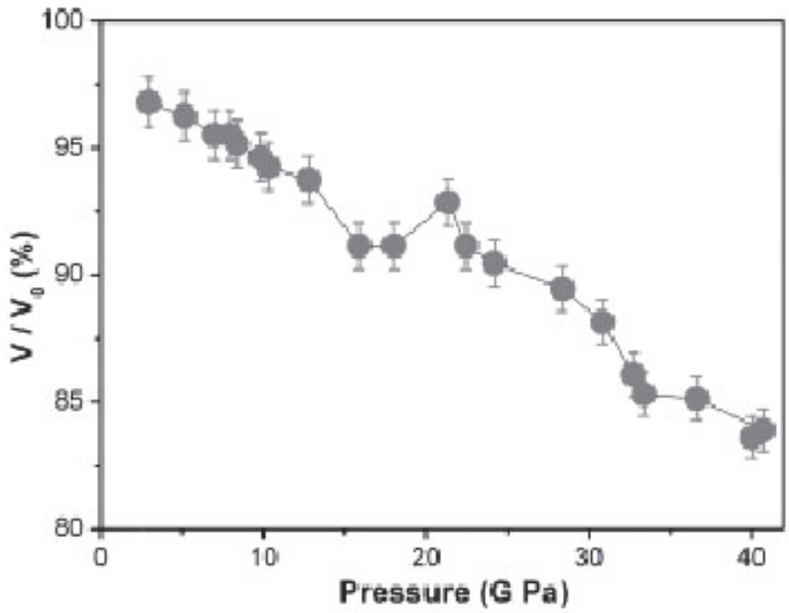

Fig. 14. The curves of the relative volume V/V_0 vs. pressure curve of 0.92PZN-0.08PT sample.

Fig.14 shows the relative volume V/V_0 vs. pressure curve of 0.92PZN-0.08PT, from which can be seen that the volume of the unit cell changes with the increasing pressure. Similar to the curve of $d_{(110)}$ vs. pressure, this curve can also demonstrate interesting multi- kinky compressive behavior. We roughly fit the experimental data to Birch-Murnaghan (BM) equation and get the equation of state (EOS) of 0.92PZN-0.08PT as following:

$$P = \frac{3}{2}B_0\left[\left(\frac{V}{V_0}\right)^{-\frac{7}{3}} - \left(\frac{V}{V_0}\right)^{-\frac{5}{3}}\right] * \left\{1 - \frac{3}{4}\left(4 - B_0^1\right) \times \left[\left(\frac{V}{V_0}\right)^{-\frac{2}{3}} - 1\right]\right\} \tag{4}$$

the bulk modulus B_0 and its first-order derivative B_0^1 for 0.92PZN-0.08PT system are obtained as $B_0 = 267 \pm 15$GPa, $B_0^1 = 4$.

As shown in Fig.13 and Fig.14, the structure parameters (d and V) display several abrupt changes around several crossover pressures (or during several pressure ranges), which are the suggestive of the anomalous phase transitions and multi-kinky compressive behavior of 0.92PZN-0.08PT crystals under high-pressure condition. It is speculated that this kinky behavior of the structural parameters of 0.92PZN-0.08PT could also be a more general feature in ABO_3-type perovskite oxides. For instance, some similar anomalous behaviors had also been presented in $BaTiO_3$ and $PbTiO_3$.[20] Through the calculations using a first-principles approach based on density-functional theory, an enormous tetragonal strain can be induced in these two simple perovskites by application of a negative hydrostatic pressure. Their structural parameters such as cell volume and atomic displacements were found to display a kinky behavior suggestive of proximity to a phase transition. Comparatively, in the present work, a multi-kinky compressive behavior in 0.92PZN-0.08PT which is more complex than single kinky behavior appeared in $BaTiO_3$ and $PbTiO_3$ was obtained. In a way, the different compressive behavior between 0.92PZN-0.08PT and the

simple peroveskites may be ascribed to the chemical composition variation. The *B* cation of $BaTiO_3$ and $PbTiO_3$ is only comprised by Ti^{4+} ion, while that of 0.92PZN-0.08PT is comprised by Zn^{2+}, Nb^{5+}, and Ti^{4+} ions, which makes the structure of 0.92PZN-0.08PT more complex than that of $BaTiO_3$ and $PbTiO_3$.

The unique nonlinear behavior in 0.92PZN-0.08PT can also be explained in terms of the relative compressibilities of the octahedral (BO_6 polyhedral) and dodecahedral (AO_{12} polyhedral) cation sites in the perovskites structure, or of the compressibilities of the *A*-O and *B*-O bonds, as shown in Fig.10. It is clearly that the relative compressibilities of the AO_{12} and BO_6 sites must play an important role in determining whether the perovskite structure becomes more or less distorted with increasing pressure.[22] From the curves of cell volume or d-spacing Vs pressure, we found that the bulk compressibilities in 0.92PZN-0.08PT varying with applying pressures. Since 0.92PZN-0.08PT is of perovskite structure comprised by AO_{12} and BO_6 polyhedra, we think the evolution of the bulk compressibilities in it can also be ascribed to the relative compressibilities of the AO_{12} and BO_6.

The so-called polyhedral approach is based on the observation that the identification of cation–oxygen polyhedra, M_xO_y, not only simplifies the description of complex crystal structures, but also allows a better understanding of physical properties for materials containing similar polyhedra.[23,24] Considering the influence of the bond length and the anion/cation charge of a given polyhedron on the compressibility, the empirical expression for the compressibility of a given polyhedron were derived:

$$K_{poly} = \frac{4}{3}\frac{d^3}{S^2 Z_0 Z_a} GPa^{-1} \tag{5}$$

Z_a is the anion charge, Z_0 the cation charge, d the bond length in Å and S^2 an ionicity scaling factor equal to 1/2 for oxygen-based polyhedra. The extension of this approach is to assume that the compressibility of complex crystals with linked polyhedra can be derived when κ_{poly} for each polyhedron is known. Based on the consideration of the influence of cation–anion distances and angles between polyhedra (polyhedra tilting), J. Kresiel et al proposed a simple model to deduce the bulk compressibility, κ_{bulk}, from the compressibility of each constituent polyhedron:

$$K_{bulk} = \sum_i x_i \frac{V_i}{V_0} k_i^{poly} \tag{6}$$

where the index i refers to a given type of cation–anion polyhedron and x_i is the concentration on a crystallographic site. V_i and V_0 are the volumes of a given polyhedron and the unit cell, as described by

$$\sum_i \left(x_i \frac{V_i}{V_0} \right) = 1 \tag{7}$$

Since in PZN-PT crystal, the AO_{12} polyhedron is PbO_{12} dodecahedra and the BO_6 polyhedra is comprised by Zn-O group, Nb-O group, and Ti- O group. The equation (6) was modified to estimate the compressive behavior of 0.92PZN-0.08PT as following:

$$K_{PZNT} = \frac{V_{PbO12}}{V_{PZNT}} + x\frac{V_{ZnO6}}{V_{PZNT}} + y\frac{V_{NbO6}}{V_{PZNT}} + z\frac{V_{TiO6}}{V_{PZNT}} \tag{8}$$

where x, y, z implies the concentration of Pb^{2+}, Zn^{2+}, Nb^{5+}, and Ti^{4+} ions, respectively. Due to these cations being chemically very different, it is believed that the compessibilities of these MO_6 polyhedra will be different on applying various pressures, which influence the total compressibilities in 0.92PZN-0.08PT crystals. Therefore, although this high-pressure diffraction technique only allow the determination of the mean bond distance, *d*, averaged over the entire crystal for each distinct polyhedron, the modified model can be considered as an approach to explain the compressive behavior and the change of compressibilities of 0.92PZN-0.08PT crystal under high-pressure conditions.

Therefore, through the method of high pressure synchrotron radiation energy-dispersive x-ray diffraction, the abnormal compressive behavior in 0.92PZN-0.08PT under high-pressure have been observed, which is considered to be intimately related to the structural characteristics of 0.92PZN-0.08PT crystals. The high-pressure compressive behavior reflects and uncovers abundant structural information under extreme conditions, which is helpful to intrigue significant interests in exploring the structural nature and chemical (or physical) origin of ultrahigh performance in relaxor ferroelecric materials and other functional materials.

2.3 XAFS study in relaxor ferroelectrics

Relaxor ferroelectrics are a class of ferroelectrics that have a diffuse, frequency-dependent permittivity maximum, with a relaxation spectrum much broader than the Debye type. But these features do not provide a direct link to the key structural element that is essential for relaxor ferroelectrics. A common, crucial element in all Pb containing relaxors, Pb(B′, B′′)O3, is a size mismatch between the ferroelectrically active B′′ cations and the ferroelectrically inactive B′ cations. The data of extended X-ray absorption fine structure (EXAFS) based on synchrotron radiation can provide local structural evidence in indicating the structural origin of the anomanous properties in relaxors.

2.3.1 Synchrotron radiation XAFS approach

X-ray absorption fine structure (XAFS) refers to the details of how x-rays are absorbed by an atom at energies near and above the core-level binding energies of that atom, as shown in Fig.15. Specifically, XAFS is the modulation of an atom's x-ray absorption probability due to the chemical and physical state of the atom. XAFS spectra are especially sensitive to the formal oxidation state, coordination chemistry, and the distances, coordination number and species of the atoms immediately surrounding the selected element. Because of this dependence, XAFS provides a practical and simple way to determine the chemical state and local atomic structure for a selected atomic species. XAFS can be used in a variety of systems and bulk physical environment.

X-ray absorption measurements are relatively straightforward, provided one has an intense and energy-tunable source of x-rays, such as a synchrotron radiation source. Many experimental techniques and sample conditions are available for XAFS, including such possibilities as very fast measurements of high spatial resolution. Since the characteristics of synchrotron sources and experimental station dictate what energy ranges, beam sizes, and intensities are available, this often puts practical experimental limits on the XAFS measurements that can be done even if there are few inherent limits on XAFS. The x-ray absorption spectrum is typically divided into two regimes: x-ray absorption near-edge spectroscopy (XANES) and extended x-ray absorption fine-structure spectroscopy (EXAFS).

Though the two have the same physical origin, this distinction is convenient for the interpretation. XANES is strongly sensitive to formal oxidation state and coordination chemistry (e.g., octahedral, tetrahedral coordination) of the absorbing atom, while the EXAFS is used to determine the distances, coordination number, and species of the neighbors of the absorbing atom.

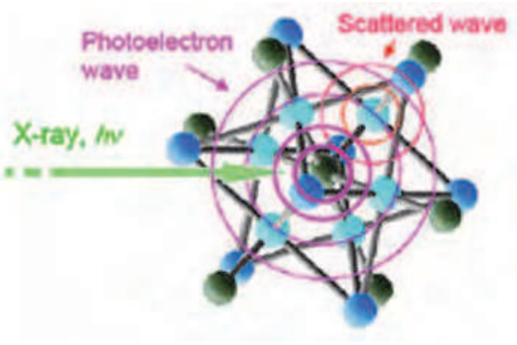

Fig. 15. (Colour on the web only) Illumination of XAFS measurements.

2.3.2 XAFS study in $Pb(Fe_{1/2}Nb_{1/2})_{1-x}Ti_xO_3$ (PFNT) relaxor crystals

Lead iron niobate $Pb(Fe_{1/2}Nb_{1/2})O_3$ (PFN) has been studied of great interest recently because of its multiferroic and relaxor ferroelectric properties. $Pb(Fe_{1/2}Nb_{1/2})_{1-x}Ti_xO_3$ (PFNT) is a modified material which has been also studied extensively in recent years. PFNT undergoes a rhombohedral-tetragonal phase transition with the increase of Ti concentration.[25] Recent study reveals that the morphotropic phase boundary (MPB) is in the range $0.06 < x < 0.08$.[26] The PFNT ceramics (x=0.13) shows a diffuse phase transition at 398 K.[27] The (001)-cut PFNT (x=0.48) single crystal undergoes a tetragonal-cubic phase transition at 518 K, but no Curie temperature was detected below 570 K in the (001)-cut PFNT (x=0.06) crystal.[28,29]

We investigated the dielectric properties of PFNT single crystals below room temperature.[30] The EXAFS results provided a clear picture of the local structure of iron ions in PFNT, and the pre-edge XAFS suggests that the observed dielectric anomaly is induced by the hopping conductivity between Fe^{2+} and Fe^{3+}. we report the low temperature (90~300 K) dielectric properties of the (100)-cut PFNT single crystals. Two dielectric anomaly induced by different mechanisms were observed in the low Ti-doped sample, while only one was detected in the high Ti-doped sample. The mechanism of the dielectric anomalies were discussed based on the microstructures investigated by X ray absorption fine structure (XAFS) results.

High quality PFNT single crystals (x=0.07, named sample A; x=0.48, named sample B) were fabricated without any impure phase. Both samples were cut with surface parallel to (100) plane. Pre-edge and extended x ray absorption fine structure (EXAFS) data were collected at the beamline 13B of Photo Factory, National High Energy Institute of Japan at room temperature. To measure the dielectric properties, aluminium electrodes were evaporated on both sides of the samples.[30]

From activation energy consideration, it seems that the A-site doping can change the activation energy values but the B-site doping can not. Considering the different B-site doping of our two samples, though the crystal structures are very different, they have the close activation energy values.[30] Fig.16 (a) shows the background-subtracted pre-edge XAFS spectra at Fe K-edge for both samples, with tree peaks (named A, B and C).

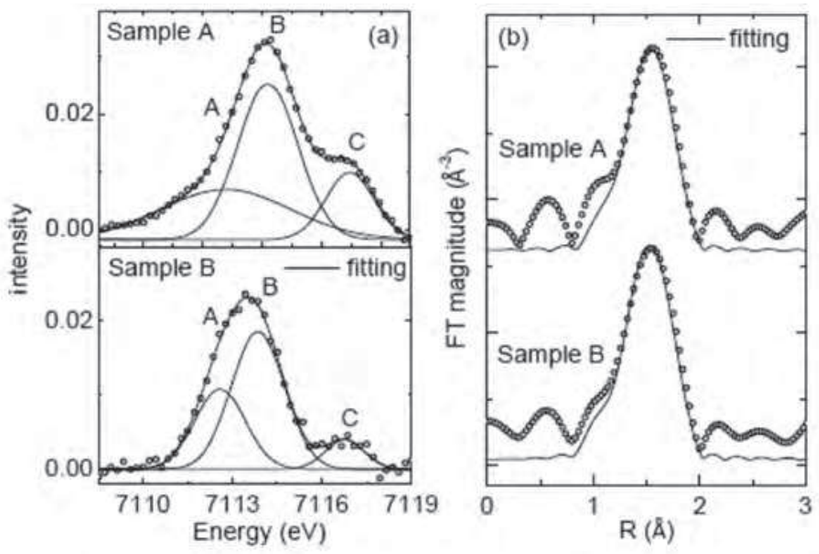

Fig. 16. (a) Pre-edge absorption spectra of Fe K edge, symbols are experiment data, and lines arefitting results by Gaussian function; (b) Fourier transform of Fe K edge (first coordinate shell), symbols are experiment data, and lines are fitting results

The experiment data is fit perfectly using three Gaussian functions. The positions of the three peaks are determined to be 7112.8, 7114.2 and 7116.9 eV for sample A, and 7112.6, 7113.9 and 7116.8 eV for sample B, respectively. All the three peaks of sample B are slightly lower energy shifted than sample A, approximately 0.1~0.3 eV. This might be due to their different crystal structures. Peak B is located around 7114 eV, which is close to the value reported for ferric compounds. The separation between peak A and peak B corresponds to the typical separation of the order of 1.4 eV that has been reported for Fe2+ and Fe3+, therefore, Fe2+ ions exist in our crystals.[30] The pre-edge XAFS suggests that the first anomaly is induced by the hopping conductivity between Fe2+ and Fe3+. The local structure of iron ions is studied by EXAFS at Fe K-edge. Fig.16(b) shows the Fourier transform of the Fe K-edge spectra for both samples. The first coordinate shell (Fe-O) is well separated and analysised, and the structure parameters are listed in Table I.

x	N	R	σ^2 (10^{-3})	E_0	R factor (%)
0.07	5.4±0.2	2.011±0.003	6	-5.5±0.5	1.1
0.48	5.7±0.1	2.007±0.005	6	-8.2±0.8	2.3

Table 1. (Colour on the web only) Parameters of the first coordinate shell of Fe K edge: N is coordinate number, R is the distance of Fe-O, σ 2 is Debye-Waller factor, E0 is energy shift, and R is relative error.

The coordinate number of both samples is smaller than 6, implying that there are oxygen vacancies in our crystals. Moreover, the sample A has a smaller coordinate number than the sample B, indicating the higher oxygen vacancy concentration of sample A than sample B, which can be also confirmed by the impedance spectra (not shown here) that sample A has much smaller resistance than sample B. The distance of Fe-O for both samples is very close.

It is worth noticing that the two samples have the close Debye-Waller (DW) factor value, implying that the local environment of iron ions in sample A is similar to that in sample B. Based on the EXAFS results, we conclude that the B-site doping hardly changes the local structure of iron ions. Thus, the electrons might need the similar energy to overcome the potential barrier to hop between Fe2+ and Fe3+, leading to the close activation energy value. On the other hand, we assume that for the A-site doping, the local structure of iron ions might be distorted significantly, and then results in the different activation energy values.

3. Conclusion

The principles for studying ferroelectric domain structure by white beam synchrotron radiation X-ray diffraction topography (WBSRT)has been introduced, and several results on dynamic behavior of domain structure and phase transition in several ferroelectric crystals induced by temperature and DC electric field had been introduced. Due to its simple principle and accessible setup, WBSRT has become a unique method to characterize ferroelectric materials. WBSRT offers an elegant solution to observe ferroelectric domain structures, to study the dynamic domain behavior and in-situ phase evolution induced by the changes of temperature, electric field, or other parameters, along with other structural study techniques it is possible to give insight into various phenomena occuring in ferroic materials. Through the method of high pressure synchrotron radiation energy-dispersive x-ray diffraction, the abnormal compressive behavior in 0.92PZN-0.08PT under high-pressure have been observed, which is considered to be intimately related to the structural characteristics of 0.92PZN-0.08PT crystals. The high-pressure compressive behavior reflects and uncovers abundant structural information under extreme conditions. The XAFS did a good job to give us a clear picture of the localized state hopping conductivity, and the similar local environment of iron ions is the origin of the close activation energy of the samples. All these will be helpful to intrigue significant interests in exploring the structural nature and chemical (or physical) origin of ultrahigh performance in relaxor ferroelecric materials and other functional materials.

4. Acknowledgment

The support of this work by the National Natural Science Foundation of China (No. 10401004), China Postdoctoral Science Foundation (No. 20040350122), and Portugal FCT project of PTDC/FIS/116146/2009 is grateful acknowledged.

5. References

[1] Eitel. R. E, Novel piezoelectric ceramics:development of high temperature, high performance piezoelectric on the basis of structure, Thesis in Department of Materials Science and Engineering, The Pennsylvania State University, 2003.

[2] Yoshikawa. S, Bogue. A, Degon. B, Commercial Application of Passive and Active piezoelectric Vibration Control, Proceedings of the *11th IEEE International Symposium on Applications of Ferroelectrics*, (eds. E. Colla, D. Damjanovic & N. Setter) Montreux, Switzerland, 1998; 29:3-4.

[3] Jaffe. B, Cook.R, Jaffe. H, *Piezoelectric Ceramics,* Academic Press, New York, (1971).

[4] Park. S. E., Shrout. T.R., J. Appl. Phys., 1997; 82: 1804.

[5] Dong. M., Ye. Z. G, J. Crystal Growth, 2000; 209: 81.
[6] David. R., Gabrielle. G., X-ray topography, NIST Recommended Practice Guide, Special publication 960-10.
[7] Huang. X, Jiang. S, Zeng. W, Hu. X, Feng. D, Appl. Phys. Lett., 1995; 66:2649.
[8] Zhao. J, Yang. P, Jiang. S, Appl. Phys. Lett., 1991; 59:1952.
[9] Cloetens. P, Boller. E, Ludwig. W, Baruchel. J, europhysics news, 2010; March:46.
[10] Jiang. J, Zhao. J, Tian. Y, Instr. and Meth., 1993; 366: 354.
[11] Xiao. J, Zhang. X, Zhu.P, Huang. W, Yuan. Q, Solid State Communication, 2008; 148: 109.
[12] Yuan. Q, Zhao. C, Luo. W, Yin. X, Journal of Crystal Growth, 2001; 233:717.
[13] Fujishiro, K.; Vlokh, R.; Kiat, J.; Dkhil, B.; Yamashita, Y. *Jpn. J. Appl. Phys.* 1998, *37*, 5246-5248.
[14] Xiao, J.; Tian, Y.; Huang, W.; Hang, Y.; Yin, S. *Phys. Lett. A*. 2002, *300*, 456-460.
[15] Paszkowicz, W. *Nuclear Instruments and Method in Physics Research B*.2002, *198*, 142-182.
[16] Kreisel, J.; Bouvier, P.; Naglione, M.; Dkhil, S. A. *Phys. Rev. B*. 2004, *69*, 090104.
[17] Kreisel, J.; Dkhil, B.; Bouvier, P.; Kiat, J. *Phys. Rev. B*. 2002, *65*, 172101.
[18] Janolin, P. E.; Dkhil, B.; Bouvier, P.; Kreisel, J.; Thomas, P. A. *Phys. Rev. B*. 2006, *73*, 094128.
[19] Liu, J.; Li, Y. *Phys.: Condens. Matter*. 2002, *14*, 10505-10509.
[20] Tinite, S.; Rabe, K.; Vanderbilt, D. *Phys. Rev. B*. 2003, *68*, 144105.
[21] Bellaiche, L.; Kunc, K.; Besson, J. *Phys. Re. B*. 1996, *54*, 8945-8959.
[22] Zhao, J.; Ross, N.; Angel, R. *Acta Crystallographica Section B*. 2004, *60*, 263-271.
[23] Hazen, R. *Rev. Mineral*. 1985, *14*, 317-346.
[24] Kreisel, J.; Glazer, A. *J. Phys.: Condens. Matter.* 2000, *12*, 9689-9698.
[25] V.V.S.S. Sai Sunder, and A. M. Umarji, Material Research Bulletin, 30, 427-434, (1995)
[26] S. P. Singh, A. K. Singh, and D. Pandey, J. Phys.: Condense Matter 19, 036217, (2007)
[27] S. P. Singh, A. K. Singh, and D. Pandey, Ferroelectrics, 324, 49 (2005)
[28] C.-S. Tu, C. T. Tseng, R. R. Chien, V. Hugo Schmidt, and C.-M. Hsieh, J Appl. Phys. 104,054106 (2008)
[29] Jie Wang, X. G. Tang, H. L. W. Chan, C. L. Choy, and Haosu Luo, Appl. Phys. Lett. 86, 152907,(2005)
[30] Kui Liu, Xinyi Zhang, Shiqiang Wei, Jingzhong Xiao, Dielectric anomalies induced by different mechanisms in Pb(Fe1/2Nb1/2)1-xTixO3 single crystals, arXiv:0810.1346(October 2008).
[31] Emiel Hensen, Qingjun Zhu, Pang-Hung Liu, Kuei-Jung Chao, and Rutger van Santen, Journal of Catalysis 226, 466–470 (2004)

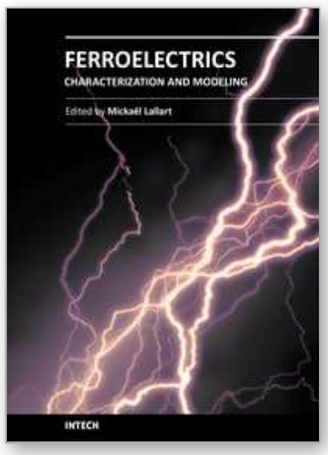

Ferroelectrics - Characterization and Modeling

Edited by Dr. MickaÃ«l Lallart

ISBN 978-953-307-455-9
Hard cover, 586 pages
Publisher InTech
Published online 23, August, 2011
Published in print edition August, 2011

Ferroelectric materials have been and still are widely used in many applications, that have moved from sonar towards breakthrough technologies such as memories or optical devices. This book is a part of a four volume collection (covering material aspects, physical effects, characterization and modeling, and applications) and focuses on the characterization of ferroelectric materials, including structural, electrical and multiphysic aspects, as well as innovative techniques for modeling and predicting the performance of these devices using phenomenological approaches and nonlinear methods. Hence, the aim of this book is to provide an up-to-date review of recent scientific findings and recent advances in the field of ferroelectric system characterization and modeling, allowing a deep understanding of ferroelectricity.

InTech Europe
University Campus STeP Ri
Slavka Krautzeka 83/A
51000 Rijeka, Croatia
Phone: +385 (51) 770 447
Fax: +385 (51) 686 166
www.intechopen.com

InTech China
Unit 405, Office Block, Hotel Equatorial Shanghai
No.65, Yan An Road (West), Shanghai, 200040, China
中国上海市延安西路65号上海国际贵都大饭店办公楼405单元
Phone: +86-21-62489820
Fax: +86-21-62489821

IntechOpen